Behavior of the collective rotor in nuclear chiral motion

Q. B. Chen,[1,*] N. Kaiser,[1,†] Ulf-G. Meißner,[2,3,4,‡] and J. Meng[5,6,§]

[1]*Physik-Department, Technische Universität München, D-85747 Garching, Germany*

[2]*Helmholtz-Institut für Strahlen- und Kernphysik and Bethe Center for Theoretical Physics, Universität Bonn, D-53115 Bonn, Germany*

[3]*Institute for Advanced Simulation, Institut für Kernphysik and Jülich Center for Hadron Physics, Forschungszentrum Jülich, D-52425 Jülich, Germany*

[4]*Ivane Javakhishvili Tbilisi State University, 0186 Tbilisi, Georgia*

[5]*State Key Laboratory of Nuclear Physics and Technology, School of Physics, Peking University, Beijing 100871, China*

[6]*Yukawa Institute for Theoretical Physics, Kyoto University, Kyoto 606-8502, Japan*

(Received 4 April 2019; published 21 June 2019)

The behavior of the collective rotor in the chiral motion of triaxially deformed nuclei is investigated using the particle rotor model by transforming the wave functions from the K representation to the R representation. The energy spectra of the doublet bands and their energy differences as functions of the triaxial deformation are first examined and then the angular momentum components of the rotor, proton, neutron, and the total system are investigated. Moreover, the probability distributions of the rotor angular momentum (R plots) and their projections onto the three principal axes (K_R plots) are analyzed. The evolution of the chiral mode from a chiral vibration at the low spins to a chiral rotation at high spins is illustrated at triaxial deformations $\gamma = 20^\circ$ and 30°.

DOI: 10.1103/PhysRevC.99.064326

I. INTRODUCTION

Nuclear chiral rotation is an exotic form of spontaneous symmetry breaking. It can occur when high-j proton states (particles) lie above the Fermi level and high-j neutron states (holes) lie below the Fermi level (or vice versa), and at the same time the nuclear core is of triaxial ellipsoidal shape [1]. The angular momenta of the valence particles and holes are aligned along the short and long axes of the triaxial core, respectively, while the angular momentum of the rotational core is aligned along the intermediate axis. The three angular momenta can be arranged to form a left-handed or a right-handed system. Such an arrangement leads to the breaking of chiral symmetry [$\chi = \mathcal{T}\mathcal{R}_2(\pi)$, with time reversal $\mathcal{T}$ and 180° degree rotation $\mathcal{R}_2(\pi)$] in the body-fixed frame. With the restoration of this symmetry in the laboratory frame, degenerate doublet $\Delta I = 1$ bands with the same parity, so-called chiral doublet bands [1], occur.

So far, more than 50 candidates for this phenomenon have been observed in odd-odd nuclei as well as in odd-A and even-even nuclei, and these are spread over the mass regions $A \approx 80$, 100, 130, and 190. For more details, see the review articles [2–7] and the corresponding data tables in Ref. [8]. With the prediction [9] and confirmation [10] of multiple chiral doublets (MχD) in a single nucleus, the investigation of nuclear chirality continues to be one of the hottest topic in modern nuclear physics [11–33].

By now it is well known that chiral rotations (aplanar rotations of the total angular momentum) can exist only above a critical spin I, see Refs. [23,32,34–37]. Actually, at low spins a chiral vibration, understood as an oscillation of the total angular momentum between the left- and right-handed configurations, happens. This suggests that the orientation of the angular momenta of the rotor, the particle(s), and the hole(s) are coplanar near the bandhead of a chiral band. This feature is caused by the fact that the angular momentum of the rotor is much smaller than those of the proton and the neutron near the bandhead [32]. On the other hand, at high spin, a chiral rotation occurs, which is driven by the increase of the rotor angular momentum along the intermediate axis.

Obviously, the rotor plays an essential role in the evolution of the chiral mode from chiral vibration to chiral rotation. Therefore, the detailed exploration of the behavior of the collective rotor in nuclear chiral motion is of high interest. Previously, such investigations were mainly carried out by calculating expectation values of components of the rotor angular momentum [15,16,22,38–42]. Only rare attempts have been made to investigate the detailed wave functions of the collective rotor in chiral bands. To our knowledge only in Ref. [14] have the rotor wave functions been explored at the beginning and the end of chiral bands.

In this work we will take the system of one $h_{11/2}$ proton particle and one $h_{11/2}$ neutron hole coupled to a triaxial rigid rotor as a concrete example to investigate systematically the behavior of the collective rotor angular momentum in nuclear chiral motion.

*qbchen@pku.edu.cn
†nkaiser@ph.tum.de
‡meissner@hiskp.uni-bonn.de
§mengj@pku.edu.cn

Among various nuclear models, the particle rotor model (PRM) has been widely used to describe chiral doublet bands with different kinds of particle-hole configurations [1,10,18,20,22,26,28,32,38–51]. It is a quantum mechanical model, which treats the collective rotation and the intrinsic single-particle motions based on a description of the system in the laboratory frame. The pertinent Hamiltonian is diagonalized with total angular momentum I as a good quantum number, and the energy splittings and tunneling probabilities between doublet bands can be obtained directly from the eigenvalues and eigenfunctions.

Usually, the PRM Hamiltonian is diagonalized in the strong coupling basis [52,53], where the projection of the total spin onto the 3-axis of the intrinsic frame is a good quantum number, denoted by K. In this K representation, the rotor angular momentum R and its three possible projections K_R onto the intrinsic axes do not appear explicitly. In order to give the proper wave function of the rotor, one has to express the PRM wave function in terms of the weak-coupling basis [52,53], in which both R and K_R are good quantum numbers. This transformation gives the R representation, and from the corresponding probability distributions one can derive the R *plot* and three K_R *plots*.

The technique to transform the PRM wave function from the K representation to the R representation is outlined in the textbook [52]. In particular, we have used it in Ref. [54] to investigate the behavior of the collective rotor in the wobbling motion of ^{135}Pr. In the present work, we extend the same method to investigate chiral bands based on a two-quasiparticle configuration.

II. THEORETICAL FRAMEWORK

A. Particle rotor Hamiltonian

In the particle rotor model (PRM) the Hamiltonian for a system with one proton and one neutron coupled to a triaxial rigid rotor is composed as [1,38,39,43,44]

$$\hat{H}_{\rm PRM} = \hat{H}_{\rm coll} + \hat{H}_p + \hat{H}_n, \tag{1}$$

where $\hat{H}_{\rm coll}$ represents the Hamiltonian of the rigid rotor,

$$\hat{H}_{\rm coll} = \sum_{k=1}^{3} \frac{\hat{R}_k^2}{2\mathcal{J}_k} \tag{2}$$

$$= \sum_{k=1}^{3} \frac{(\hat{I}_k - \hat{j}_{pk} - \hat{j}_{nk})^2}{2\mathcal{J}_k}, \tag{3}$$

with the index $k = 1, 2, 3$ denoting the three principal axes in the body-fixed frame. Here, $\hat{R}_k$ and $\hat{I}_k$ are the angular momentum operators of the collective rotor and the total nucleus, while $\hat{j}_{p(n)k}$ is the angular momentum operator of the valence proton (neutron). Moreover, the parameters $\mathcal{J}_k$ are the three principal moments of inertia. When calculating matrix elements of $\hat{H}_{\rm coll}$, the R representation is most conveniently used for its form in Eq. (2), while the form in Eq. (3) is preferably treated in the K representation.

The Hamiltonians $\hat{H}_p$ and $\hat{H}_n$ describe the single proton and neutron outside of the rotor. For a nucleon in a single-j shell orbital, it is given by

$$\hat{H}_{p(n)} = \pm\frac{1}{2}C\left\{\cos\gamma\left[\hat{j}_3^2 - \frac{j(j+1)}{3}\right] + \frac{\sin\gamma}{2\sqrt{3}}(\hat{j}_+^2 + \hat{j}_-^2)\right\}, \tag{4}$$

where the plus sign refers to a particle and the minus sign to a hole and the angle γ serves as a triaxial deformation parameter. The coupling parameter C is proportional to the quadrupole deformation parameter β of the rotor.

B. Basis transformation from K representation to R representation

The PRM Hamiltonian in Eq. (1) is usually solved by diagonalization in the strong-coupling basis (K representation) [52,53]

$$\begin{aligned}|j_p\Omega_p j_n\Omega_n K, IM\rangle &= \sqrt{\frac{1}{2}}[|j_p\Omega_p\rangle|j_n\Omega_n\rangle|IMK\rangle \\ &\quad + (-1)^{I-j_p-j_n}|j_p-\Omega_p\rangle|j_n-\Omega_n\rangle|IM-K\rangle],\end{aligned} \tag{5}$$

where I denotes the total angular momentum quantum number of the odd-odd nuclear system (rotor plus proton and neutron) and M refers to the projection onto the 3-axis of the laboratory frame. Furthermore, $\Omega_{p(n)}$ is the quantum number for the 3-axis component of the valence nucleon angular momentum operator $\boldsymbol{j}_{p(n)}$ in the intrinsic frame, while the states $|IMK\rangle$ are represented in terms of Euler angles $\boldsymbol{\omega} = (\psi', \theta', \phi')$ by the usual Wigner functions as $\langle\boldsymbol{\omega}|IMK\rangle = \sqrt{\frac{2I+1}{8\pi^2}}D^I_{MK}(\boldsymbol{\omega})$. Under the requirement of the D_2 symmetry of a triaxial nucleus [52], K and Ω_p take the values $K = -I, \ldots, I$ and $\Omega_p = -j_p, \ldots, j_p$. The quantum number Ω_n goes over the range $\Omega_n = -j_n, \ldots, j_n$ and it has to fulfill the condition that $K_R = K - \Omega_p - \Omega_n$ is a positive even integer. In the special case $K_R = 0$, only positive values $\Omega_n = 1/2, \ldots, j_n$ are allowed. With these choices, the dimension of the Hamiltonian matrix is $(2I+1)(2j_p+1)(2j_n+1)/4$.

In the K representation (5), the rotor angular momentum quantum number R does not appear explicitly. In order to obtain the wave function of the rotor in the R representation, one has to change the basis. The details of this orthogonal transformation for a triaxial system with odd particle number can be found in Refs. [54–56]. Following the procedure presented in Ref. [54], we will extend it here to an odd-odd nucleus.

The rotational wave function of the total nuclear system in the laboratory frame can be expressed in the R representation as

$$\begin{aligned}|j_p j_n(J_{pn})RK_R, IM\rangle &= \sum_{M_{pn},M_R}\langle J_{pn}M_{pn}RM_R|IM\rangle|J_{pn}M_{pn}\rangle|RM_R\tau\rangle \\ &= \sum_{M_{pn},M_R,m_p,m_n}\langle J_{pn}M_{pn}RM_R|IM\rangle \\ &\quad\times\langle j_p m_p j_n m_n|J_{pn}M_{pn}\rangle|j_p m_p\rangle|j_n m_n\rangle|RM_R\tau\rangle,\end{aligned} \tag{6}$$

where first the coupling of $\boldsymbol{j}_p$ and $\boldsymbol{j}_n$ to $\boldsymbol{J}_{pn}$ is performed and after that $\boldsymbol{J}_{pn}$ and the rotor quantum number $\boldsymbol{R}$ are coupled to total angular momentum $\boldsymbol{I}$. In the above expression, M_R, M_{pn}, and $m_{p(n)}$ are the projection quantum numbers of $\boldsymbol{R}$, $\boldsymbol{J}_{pn}$, and $\boldsymbol{j}_{p(n)}$ on the 3-axis in the laboratory frame, respectively. Obviously, the appearance of Clebsch-Gordan coefficients requires $M = M_{pn} + M_R = m_p + m_n + M_R$. The value of J_{pn} lies in the range $|j_p - j_n| \leqslant J_{pn} \leqslant j_p + j_n$. Accordingly, for a given J_{pn}, the value of R must satisfy the triangular condition $|I - J_{pn}| \leqslant R \leqslant I + J_{pn}$ of angular momentum coupling. The additional quantum number τ refers to the projection of $\boldsymbol{R}$ onto a specific body-fixed axis.

Now we perform the transformation from the R representation to the K representation. In the K representation, the quantum number τ is identified with the projection K_R of $\boldsymbol{R}$ onto a principal axis. Making use of Wigner functions, the wave functions of the two particles and the rotor in Eq. (6) can be written as

$$|j_p m_p\rangle = \sum_{\Omega_p=-j_p}^{j_p} D^{j_p}_{m_p\Omega_p}(\boldsymbol{\omega})|j_p\Omega_p\rangle, \tag{7}$$

$$|j_n m_n\rangle = \sum_{\Omega_n=-j_n}^{j_n} D^{j_n}_{m_n\Omega_n}(\boldsymbol{\omega})|j_n\Omega_n\rangle, \tag{8}$$

$$|RM_RK_R\rangle = \sqrt{\frac{2R+1}{16\pi^2\left(1+\delta_{K_R0}\right)}} \times \left[D^R_{M_RK_R}(\boldsymbol{\omega}) + (-1)^R D^R_{M_R-K_R}(\boldsymbol{\omega})\right], \tag{9}$$

where, as mentioned already above, K_R is an even integer ranging from 0 to R, with $K_R = 0$ excluded for odd R. Both restrictions come from the D_2 symmetry of a triaxial nucleus [52].

Substituting Eqs. (7)–(9) into Eq. (6), one obtains

$$|j_p j_n(J_{pn})RK_R, IM\rangle = \sum_{K,\Omega_p,\Omega_n} A^{IK,J_{pn}\Omega_{pn}}_{j_p\Omega_p j_n\Omega_n,RK_R}|j_p\Omega_p j_n\Omega_n K, IM\rangle, \tag{10}$$

with the expansion coefficients

$$A^{IK,J_{pn}\Omega_{pn}}_{j_p\Omega_p j_n\Omega_n,RK_R} = \sqrt{\frac{2R+1}{2I+1}}\sqrt{1+\delta_{K_R,0}} \times \langle j_p\Omega_p j_n\Omega_n|J_{pn}\Omega_{pn}\rangle\langle J_{pn}\Omega_{pn}RK_R|IK\rangle. \tag{11}$$

Obviously, the transformation between the K and R representations is an orthogonal transformation, and therefore the expansion coefficients satisfy the relations

$$\sum_{K,\Omega_p,\Omega_n,\Omega_{pn}} A^{IK,J_{pn}\Omega_{pn}}_{j_p\Omega_p j_n\Omega_n,RK_R} A^{IK,J_{pn}\Omega_{pn}}_{j_p\Omega_p j_n\Omega_n,R'K'_R} = \delta_{RR'}\delta_{K_RK'_R}, \tag{12}$$

$$\sum_{R,K_R,J_{pn},\Omega_{pn}} A^{IK,J_{pn}\Omega_{pn}}_{j_p\Omega_p j_n\Omega_n,RK_R} A^{IK',J_{pn}\Omega_{pn}}_{j_p\Omega'_p j_n\Omega'_n,RK_R} = \delta_{\Omega_p\Omega'_p}\delta_{\Omega_n\Omega'_n}\delta_{KK'}. \tag{13}$$

Due to the orthogonality property, the inverse transformation follows immediately as

$$|j_p\Omega_p j_n\Omega_n K, IM\rangle = \sum_{R,K_R,J_{pn},\Omega_{pn}} A^{IK,J_{pn}\Omega_{pn}}_{j_p\Omega_p j_n\Omega_n,RK_R}|j_p j_n(J_{pn})RK_R, IM\rangle. \tag{14}$$

With this formula, we have successfully transformed the PRM basis functions from the K representation to the R representation.

The advantage of the basis states in Eq. (14) is a more convenient calculation of the matrix elements of the collective rotor Hamiltonian

$$\begin{aligned}&\langle j_p\Omega'_p j_n\Omega'_n K', IM|\hat{H}_{\rm coll}|j_p\Omega_p j_n\Omega_n K, IM\rangle \\ &= \sum_{R',K'_R,J'_{pn},\Omega'_{pn}}\sum_{R,K_R,J_{pn},\Omega_{pn}} A^{IK',J'_{pn}\Omega'_{pn}}_{j_p\Omega'_p j_n\Omega'_n,R'K'_R} A^{IK,J_{pn}\Omega_{pn}}_{j_p\Omega_p j_n\Omega_n,RK_R} \\ &\quad\times\langle j_p j_n(J'_{pn})RK'_R, IM|\hat{H}_{\rm coll}|j_p j_n(J_{pn})RK_R, IM\rangle \\ &= \sum_{R,K_R,K'_R,J_{pn},\Omega_{pn},\Omega'_{pn}} A^{IK',J_{pn}\Omega'_{pn}}_{j_p\Omega_p j_n\Omega_n,RK'_R} A^{IK,J_{pn}\Omega_{pn}}_{j_p\Omega_p j_n\Omega_n,RK_R} \\ &\quad\times\left(\sum_i c^{Ri}_{K'_R} E_{Ri} c^{Ri}_{K_R}\right).\end{aligned} \tag{15}$$

The energy eigenvalues E_{Ri} and corresponding expansion coefficients $c^{Ri}_{K_R}$ (i labels the different eigenstates) are obtained by diagonalizing the collective rotor Hamiltonian $\hat{H}_{\rm coll}$ in the basis $|RM_RK_R\rangle$ introduced in Eq. (9)

$$\hat{H}_{\rm coll}|RM_Ri\rangle = E_{Ri}|RM_Ri\rangle, \tag{16}$$

$$|RM_Ri\rangle = \sum_{K_R} c^{Ri}_{K_R}|RM_RK_R\rangle. \tag{17}$$

Most importantly, the transformation (14) allows us also to calculate the probability distributions of the rotor angular momentum, which will be given in the following section.

C. R plots and K_R plots

With the above preparations, the PRM eigenfunctions can be expressed as

$$\begin{aligned}|IM\rangle &= \sum_{K,\Omega_p,\Omega_n} d_{K,\Omega_p,\Omega_n}|j_p\Omega_p j_n\Omega_n K, IM\rangle \\ &= \sum_{K,\Omega_p,\Omega_n} d_{K,\Omega_p,\Omega_n}\sum_{R,K_R,J_{pn},\Omega_{pn}} A^{IK,J_{pn}\Omega_{pn}}_{j_p\Omega_p j_n\Omega_n,RK_R} \\ &\quad\times\sum_{M_{pn},M_R,m_p,m_n}\langle J_{pn}M_{pn}RM_R|IM\rangle \\ &\quad\times\langle j_p m_p j_n m_n|J_{pn}M_{pn}\rangle|j_p m_p\rangle|j_n m_n\rangle|RK_RM_R\rangle,\end{aligned} \tag{18}$$

where the expansion coefficients d_{K,Ω_p,Ω_n} are obtained by diagonalizing the total PRM Hamiltonian in Eq. (1). Hence, the probabilities for given R and K_R are calculated as

$$P_{R,K_R} = \sum_{J_{pn}}\left(\sum_{K,\Omega_p,\Omega_n,\Omega_{pn}} d_{K,\Omega_p,\Omega_n} A^{IK,J_{pn}\Omega_{pn}}_{j_p\Omega_p j_n\Omega_n,RK_R}\right)^2, \tag{19}$$

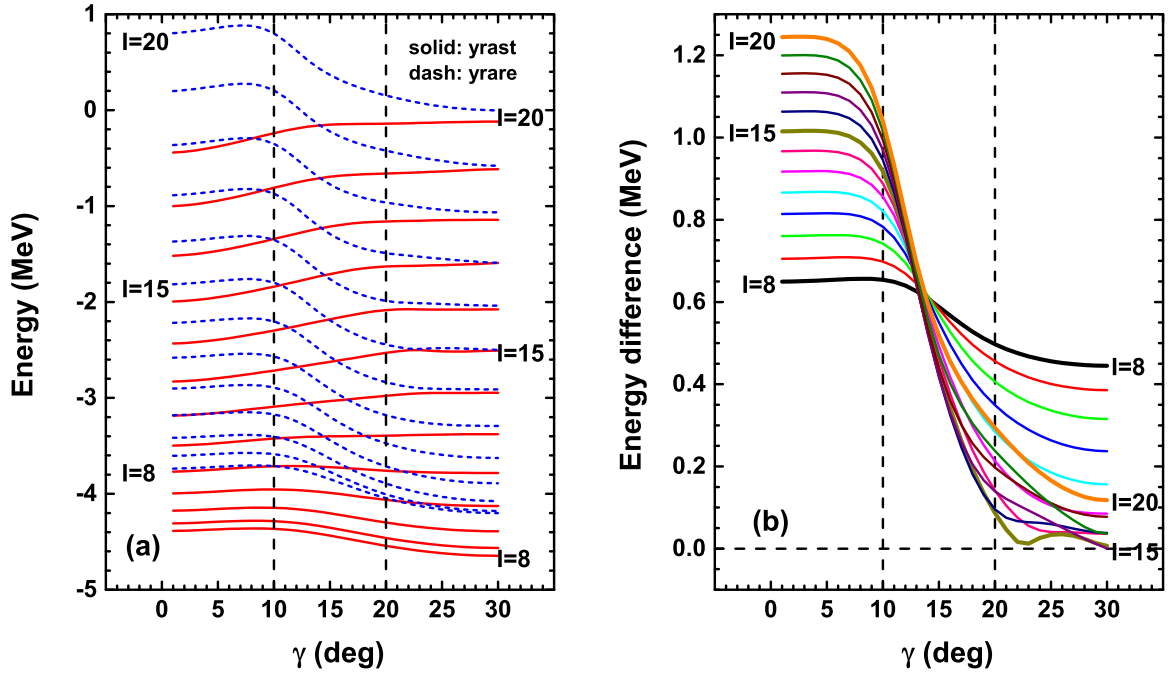

FIG. 1. (a) Energy spectra of the yrast and yrare bands for the $\pi(1h_{11/2}) \otimes \nu(1h_{11/2})^{-1}$ configuration calculated in the PRM as a function of triaxial deformation parameter γ. (b) Energy differences between the yrare and yrast bands as a function of γ.

and they satisfy the normalization condition

$$\sum_{R,K_R} P_{R,K_R} = 1. \tag{20}$$

The R plot is obtained from the summed probabilities

$$P_R = \sum_{K_R} P_{R,K_R}, \tag{21}$$

whereas in the K_R plot the probabilities are summed differently

$$P_{K_R} = \sum_{R} P_{R,K_R}. \tag{22}$$

Moreover, the expectation value of the squared angular momentum operator $\hat{R}_3^2$ follows as

$$\langle IM|\hat{R}_3^2|IM\rangle = \sum_{R,K_R} K_R^2 P_{R,K_R}. \tag{23}$$

III. NUMERICAL DETAILS

In our calculation, a system of one $h_{11/2}$ proton particle and one $h_{11/2}$ neutron hole coupled to a triaxial rigid rotor with quadruple deformation parameters $\beta = 0.23$ and triaxial deformation parameter $\gamma \in [0°, 30°]$ is considered for the purpose of illustrating the angular momentum geometry. With this assignment of γ, the 1-, 2-, and 3-axes are the intermediate (i), short (s), and long (l) axes of the ellipsoid, respectively. Moreover, moments of inertia of the irrotational flow type $\mathcal{J}_k = \mathcal{J}_0 \sin^2(\gamma - 2k\pi/3)$ $(k = 1, 2, 3)$ with $\mathcal{J}_0 = 30\ \hbar^2/\text{MeV}$ are used.

IV. RESULTS AND DISCUSSION

A. Energy spectra

The calculated energy spectra of the yrast and yrare bands for the configuration $\pi(1h_{11/2}) \otimes \nu(1h_{11/2})^{-1}$ as well as their energy differences are shown as a function of triaxial deformation parameter γ in Figs. 1(a) and 1(b) in the spin region $8\hbar \leqslant I \leqslant 20\hbar$.

For $\gamma \leqslant 10°$, the energy spectra of both yrast and yrare bands do not vary significantly. Correspondingly, their energy differences at each spin are almost constant, in particular for $\gamma \leqslant 5°$.

For $10° \leqslant \gamma \leqslant 20°$, the energy spectra of the yrast and yrare bands are sensitive to γ and show a different behavior. For the yrast band, one sees a slightly decreasing behavior for spins $8\hbar \leqslant I \leqslant 11\hbar$, and an increasing behavior for $I \geqslant 12\hbar$. In contrast to this, the yrare band decreases in the entire spin region, showing a stronger decrease at high spins. Such a behavior of the yrast and yrare bands causes the doublet bands to come close together, and hence their energy differences decrease dramatically. For example, the energy difference at $I = 20\hbar$ decreases from about 1.0 MeV to about 0.3 MeV if γ is varied from 10° to 20°. One observes that all curves cross at $\gamma \approx 13°$, which indicates that at this triaxial deformation the energy difference between the doublet bands does not change much with the spin.

For $20° \leqslant \gamma \leqslant 30°$, only a slight variation of the energy spectra of the yrast and yrare bands is observed. This feature narrows further the energy gap between the doublet bands, making them more degenerate. Actually, it becomes difficult to identify two separated rotational bands in the spin region $12\hbar \leqslant I \leqslant 20\hbar$ when γ reaches 30°, since the energy differences are less than 200 keV. In many publications

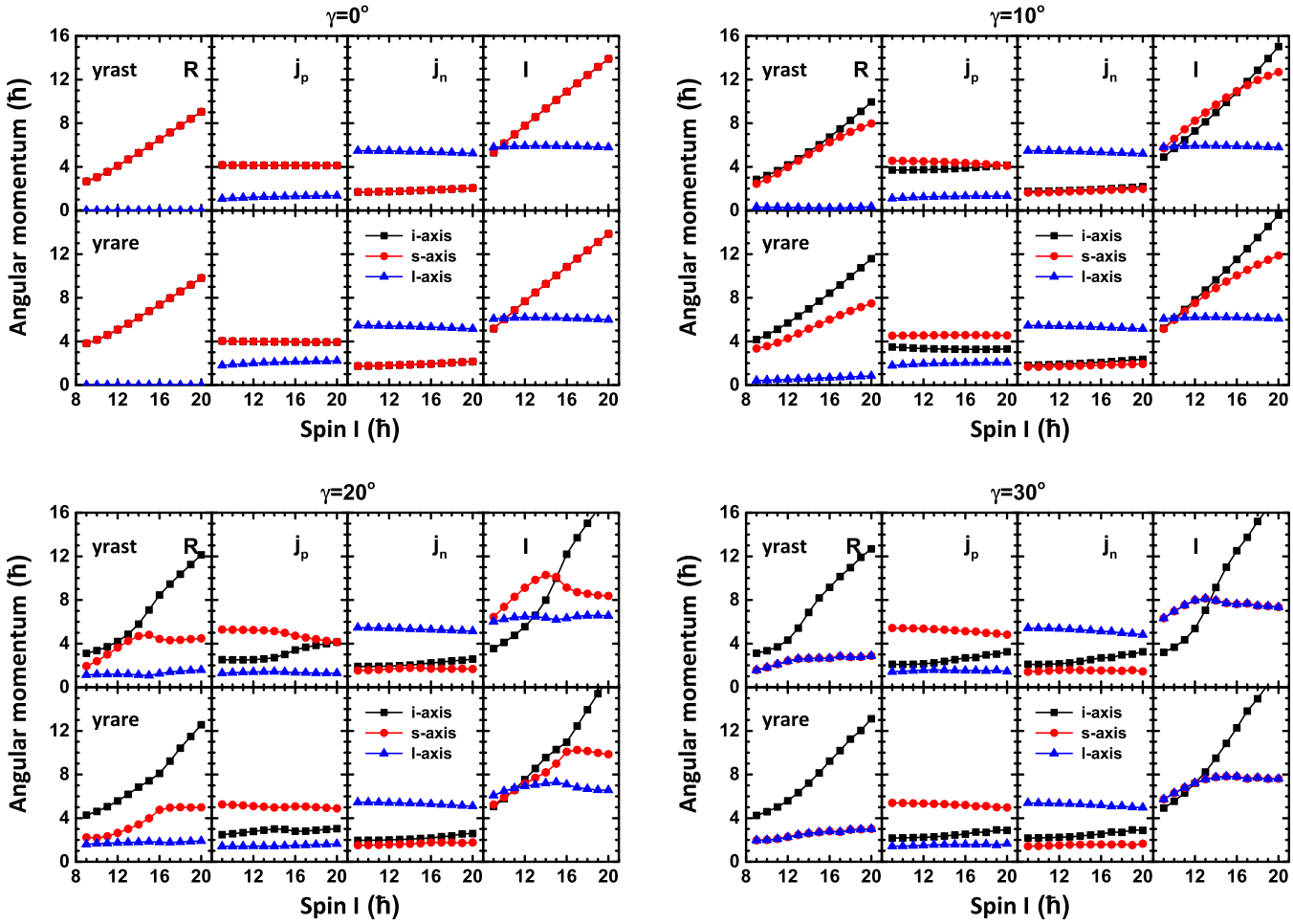

FIG. 2. Root mean square values of angular momentum components along the intermediate (i), short (s), and long (l) axes of the rotor, proton, neutron, and the total spin for the yrast and yrare bands calculated in the PRM at $\gamma = 0°$, $10°$, $20°$, and $30°$.

[1,26,32,40], $\gamma = 30°$ is considered as an ideal condition for the existence of chiral rotation for the symmetric particle-hole configuration $\pi(1h_{11/2}) \otimes \nu(1h_{11/2})^{-1}$. Here, one observes from Fig. 1(b) an approximate degeneracy and hence the condition for chiral rotation is fulfilled also at $\gamma \approx 23°$ for $I = 15\hbar$.

B. Angular momenta

In the following, the angular momentum geometries of the doublet bands are investigated by considering the situations at $\gamma = 0°$, $10°$, $20°$, and $30°$. In Fig. 2, the angular momentum components along the intermediate (i), short (s), and long (l) axes of the rotor ($\boldsymbol{R}$), proton ($\boldsymbol{j}_p$), neutron ($\boldsymbol{j}_n$), and the total spin ($\boldsymbol{I}$) for the yrast and yrare bands calculated in the PRM are shown for $\gamma = 0°$, $10°$, $20°$, and $30°$.

For $\gamma = 0°$, the deformation of the rotor is prolate. The lengths of the s and i axes and the corresponding principal moments of inertia are identical, while the moment of inertia with respect to the l axis vanishes. Therefore, the angular momentum components along the s and i axes are identical, and the collective rotation cannot happen about the l axis. This is exhibited clearly in Fig. 2. Note that due to the axial symmetry of the prolate nuclear shape with respect to the l axis, the motion of the system is a planar rotation. Two orthogonal axes, that can be freely chosen at $\gamma = 0°$, have the same angular momentum components (s and i components of the rotor angular momentum). They increase linearly with the spin I, whereas for the proton and neutron the angular momentum components remain almost constant. The proton particle is mainly aligned along the s and i axes, while the neutron hole aligns along the l axis. With these features, the components of the total spin $\boldsymbol{I}$ along the s and i axes also increase linearly, and the component along the l axis stays constant. Moreover, the components of the rotor angular momentum are different in the yrast and yrare bands. This behavior leads to the large energy difference between the doublet bands, as shown in Fig. 1.

When deviating from the prolate deformation, the nuclear shape becomes slightly triaxial. The three principal axes of the ellipsoid have different lengths, and to each corresponds a finite moment of inertia. This makes collective rotations about any of the three axes possible. For $\gamma = 10°$, the l axis component of the rotor angular momentum is small due to the small moment of inertia. For the rotor, the components R_s and R_i are similar at the low spins in the yrast band, but these

two components are different from the bandhead upward in the yrare band. For the proton, the components j_{ps} and j_{pi} are similar, and the l axis component is again small. For the neutron, the component j_{nl} is larger than j_{vs} and j_{vi}, which are both similar. With these properties, the s and i components of the total spin come out similar, and they are larger than the l component. One observes that due to the slight deviation from prolate deformation, the angular momentum geometry at $\gamma = 10^\circ$ does not change much in comparison to that at $\gamma = 0^\circ$. This explains why the energy spectra for $\gamma \leqslant 10^\circ$ do not vary significantly, as shown in Fig. 1.

For $\gamma = 20^\circ$, the three angular momentum components are different for both the yrast and yrare bands. As the total spin I increases, the components of $\boldsymbol{R}$ increase gradually, while $\boldsymbol{j}_p$ and $\boldsymbol{j}_n$ move gradually toward the i axis. Hence, the three angular momenta form together the geometry for aplanar rotation. The difference of orientation in the yrast and yrare bands appears to come mainly from the rotor for $I \leqslant 14\hbar$, and from the proton for $I \geqslant 17\hbar$. At $I = 15$ and $16\hbar$, the orientations of the rotor, proton, neutron, and the total angular momentum in the yrast and yrare bands become similar, and therefore their energy differences become smallest. This also explains the approximate degeneracy seen for $I = 15\hbar$ at $\gamma \approx 23^\circ$.

For $\gamma = 30^\circ$, the moments of inertia corresponding to the s and l axes are identical, and therefore $R_s = R_l$. The rotor mainly aligns along the i axis due to the largest momentum of inertia. In addition, one finds $j_{ps} = j_{nl}$, $j_{pl} = j_{ns}$, and $j_{pi} = j_{ni}$, which leads to $I_s = I_l$. Similar to the case $\gamma = 20^\circ$, the difference of orientation in yrast and yrare bands at $\gamma = 30^\circ$ occurs mainly at low spins $I \leqslant 13\hbar$. This corresponds to the picture of chiral vibration [32,40]. At $15\hbar \leqslant I \leqslant 17\hbar$, the orientations in the yrast and yrare bands are similar, and the doublet bands become almost degenerate, which leads to chiral rotation [32,40].

C. R plots

In Fig. 3 the probability distributions P_R of the rotor angular momentum (R plots) in the yrast and yrare bands for the $\pi(1h_{11/2}) \otimes \nu(1h_{11/2})^{-1}$ configuration calculated at $\gamma = 0^\circ$, 10°, 20°, and 30° are shown. One observes that with increasing total spin I, the distributions P_R shift their weights from the low R to the high R region, indicating a gradual increase of the rotor angular momentum.

At $\gamma = 0^\circ$ the quantum number R can take only even integer values since K_R must be zero, and therefore the distribution P_R is zero at odd R. The R plots for the yrast and yrare bands show a different behavior in the whole spin region $8\hbar \leqslant I \leqslant 20\hbar$. The weights at each R value as well as the positions of the maxima are different. In general, the R value with maximal weight in the yrare band is $2\hbar$ larger than that in the yrast band. Such a behavior causes a large energy difference between the doublet bands.

At $\gamma = 10^\circ$, the R plot is quite similar to that at $\gamma = 0^\circ$. There are only some very small contributions at odd R values in the high-spin region.

At $\gamma = 20^\circ$, the weights at odd R values are more substantial. This is because the energies of the rotor for odd R decrease with increasing γ and gradually become comparable to those for even R at $\gamma = 20^\circ$ [57]. For $I \leqslant 12\hbar$, the R value with maximal weight in the yrare band is still $2\hbar$ larger than that in the yrast band. For $I \geqslant 13\hbar$, the patterns of R plots for the yrast and yrare bands are quite similar but there remain recognizable differences for the detailed amplitudes. This similarity leads to the small energy differences (less than 300 keV) for the doublet bands in this spin region.

At $\gamma = 30^\circ$, the most prominent feature is that the R plots of the yrast and yrare bands are very similar for $I \geqslant 14\hbar$, concerning the distribution patterns and also the amplitudes. These properties lead to degenerated doublet bands.

D. K_R plots

In the following the probability distributions for the projections ($K_R = R_l$, R_s, and R_i) of the rotor angular momentum onto the l, s, and i axes (K_R plots) will be investigated. For $\gamma \in [0^\circ, 30^\circ]$, the l axis is the designated quantization axis. The distributions with respect to the s and i axes are obtained by taking $\gamma + 120^\circ$ and $\gamma + 240^\circ$. These γ values correspond to the equivalent sectors such that the nuclear shape remains the same, and only the principal axes get interchanged [52,53]. The K_R plots are symmetric under $K_R \to -K_R$ due to the D_2 symmetry of the triaxial nucleus.

In Fig. 4, the probability distributions for the projection of the rotor angular momentum onto the l axis P_{R_l} are shown for the yrast and yrare bands at $\gamma = 0^\circ$, 10°, 20°, and 30°.

At $\gamma = 0^\circ$, l-axis component of the rotor angular momentum vanishes. Hence, $P_{R_l} = 1$ at $R_l = 0$ for all spin states.

At $\gamma = 10^\circ$, the K_{R_l} plots are similar to those at $\gamma = 0^\circ$. There appear only some small distributions at $R_l = \pm 2\hbar$ in the high-spin region of the yrare band. This is consistent with the picture that the l-axis component of rotor angular momentum is small.

At $\gamma = 20^\circ$, the K_{R_l} distributions have weights mainly at $R_l = 0, \pm 2\hbar$, indicating a still small l-axis component of the rotor angular momentum.

For $\gamma = 30^\circ$, the K_{R_l} distribution becomes wider, and one observes nonvanishing contributions at $R_l = \pm 4\hbar$. Moreover, for $I \geqslant 14\hbar$, the distributions in the yrast and yrare bands are quite similar.

The probability distributions P_{R_s} of the component R_s are displayed in Fig. 5 for the yrast and yrare bands at $\gamma = 0^\circ$, 10°, 20°, and 30°.

For $\gamma = 0^\circ$, the distribution P_{R_s} has a wide spread with a peak around $R_s = 0\hbar$ at low spins $I = 8$ and $9\hbar$. For $I \geqslant 10\hbar$, this peak moves gradually toward large R_s values, indicating the increase of the rotor angular momentum component along the s axis. At $\gamma = 10^\circ$, the P_{R_s} distributions in the doublet bands have again a peak around $R_s = 0\hbar$ for low spins $I = 8$ and $9\hbar$. For $I \geqslant 10\hbar$, the P_{R_s} plots of the doublet bands behave differently. In the yrast band it has two distinct peaks located at nonzero R_s, whereas in the yrare band it is rather broad with a peak at $R_s = 0\hbar$. This implies a larger mean square deviation $\langle R_s^2 \rangle$ in the yrast band compared to yrare band.

At $\gamma = 20^\circ$, the P_{R_s} distributions show a more complicated behavior with increasing spin. For $I \leqslant 11\hbar$, one finds peaks around $R_s = 0\hbar$ for both yrast and yrare bands. In the region

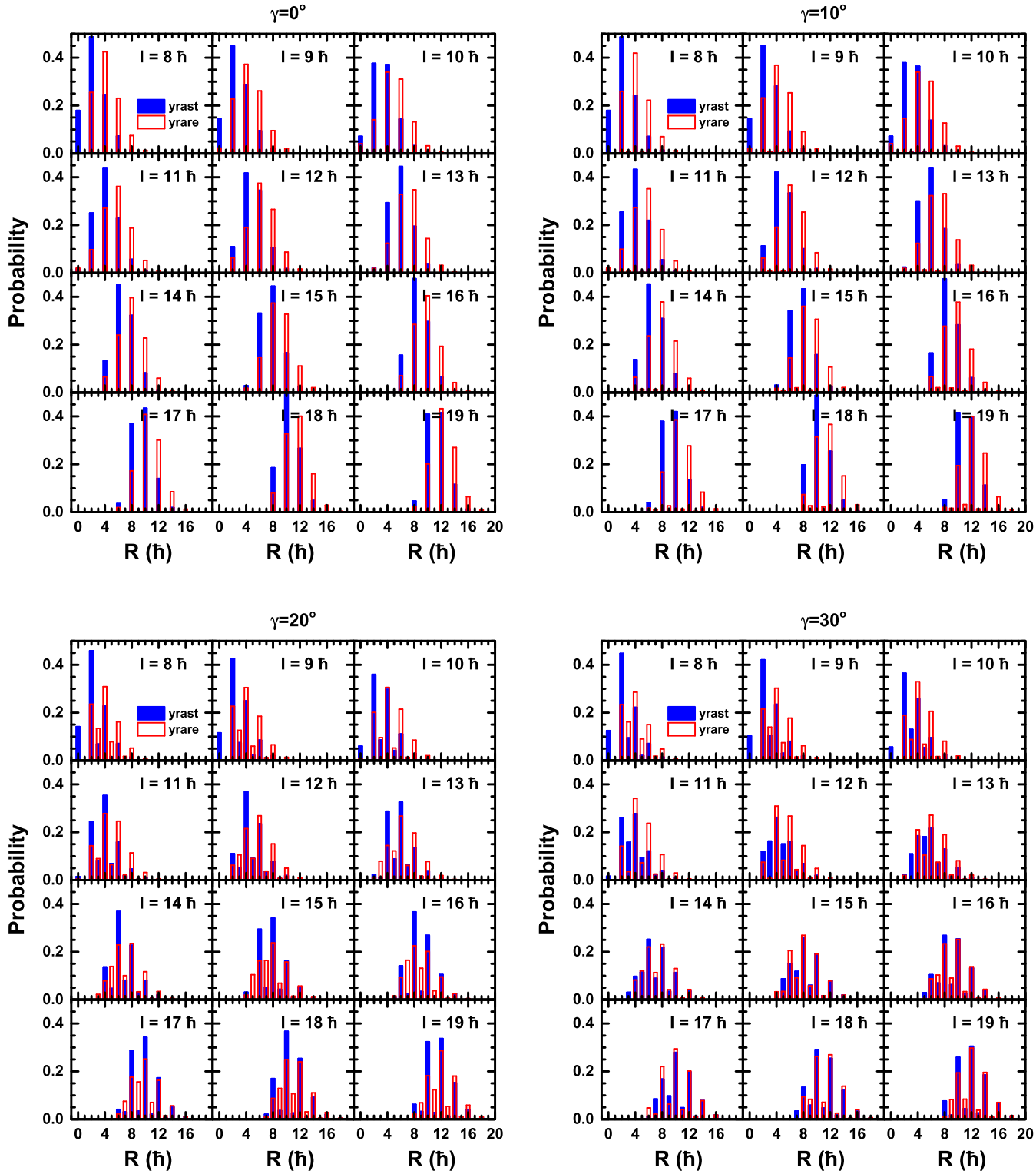

FIG. 3. R plots, probability distributions of the rotor angular momentum in the yrast and yrare bands for the $\pi(1h_{11/2}) \otimes \nu(1h_{11/2})^{-1}$ configuration calculated with the PRM at $\gamma = 0°$, $10°$, $20°$, and $30°$.

$12\hbar \leqslant I \leqslant 15\hbar$, the peak in the yrast band occurs at nonzero R_s values, while in the yrare band it stays at $R_s = 0\hbar$. For $I \geqslant 16\hbar$, the R_s plots of the yrast and yrare bands are again similar with a peak at $R_s = 0\hbar$.

At $\gamma = 30°$, the P_{R_s} and P_{R_l} distributions are the same since the moments of inertia with respect to l and s axes are identical. The P_{R_s} distributions become narrow in comparison to the other cases of triaxial deformation. The peaks located

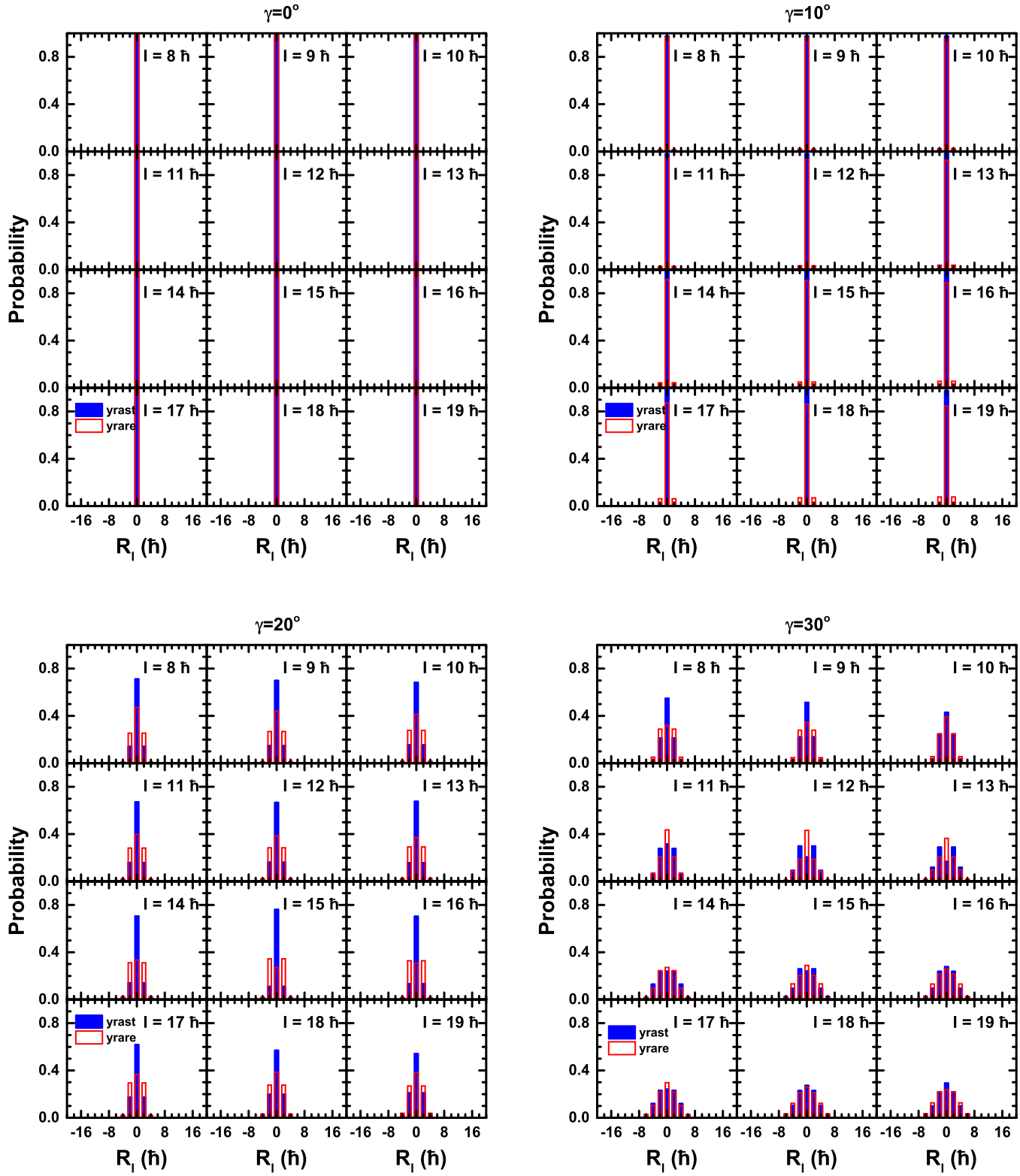

FIG. 4. K_{R_i} plots, probability distributions for the projection of the rotor angular momentum onto the l axis in the yrast and yrare bands for the $\pi(1h_{11/2}) \otimes \nu(1h_{11/2})^{-1}$ configuration calculated with the PRM at $\gamma = 0°$, $10°$, $20°$, and $30°$.

around $R_s = 0\hbar$ demonstrate the reduction of the rotor angular momentum component along the s axis, as shown by the four plots in Fig. 2.

In Fig. 6 the probability distributions P_{R_i} of the component R_i are shown for the yrast and yrare bands at $\gamma = 0°$, $10°$, $20°$, and $30°$.

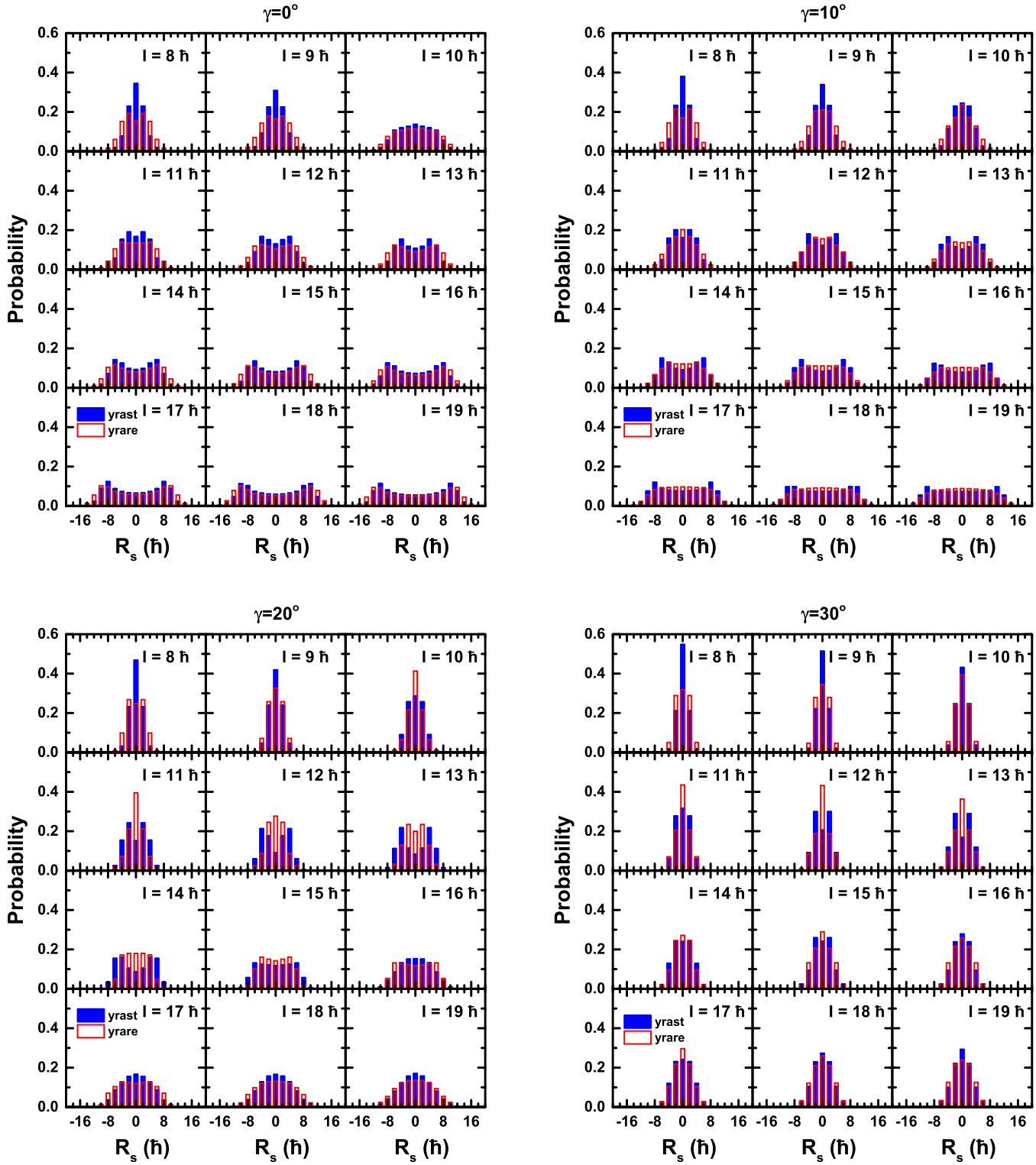

FIG. 5. Same as Fig. 4, but for the projection onto the s axis.

At $\gamma = 0^\circ$, the P_{R_i} and P_{R_s} distributions are the same since the corresponding moments of inertia are equal.

At $\gamma = 10^\circ$ the P_{R_i} distribution is similar to that at $\gamma = 0^\circ$, but the amplitude at $R_i = 0\hbar$ is a bit larger in the yrast band than in the yrare band.

At $\gamma = 20^\circ$, the P_{R_i} distribution for $I \leqslant 13\hbar$ in the yrast band has only one peak at $R_i = 0\hbar$, while that in the yrare band has two peaks at nonzero R_i. This situation corresponds to the chiral vibration. For $I \geqslant 14\hbar$, the P_{R_i} distributions for both doublet bands have two peaks at nonzero R_i, indicating the onset of chiral rotation.

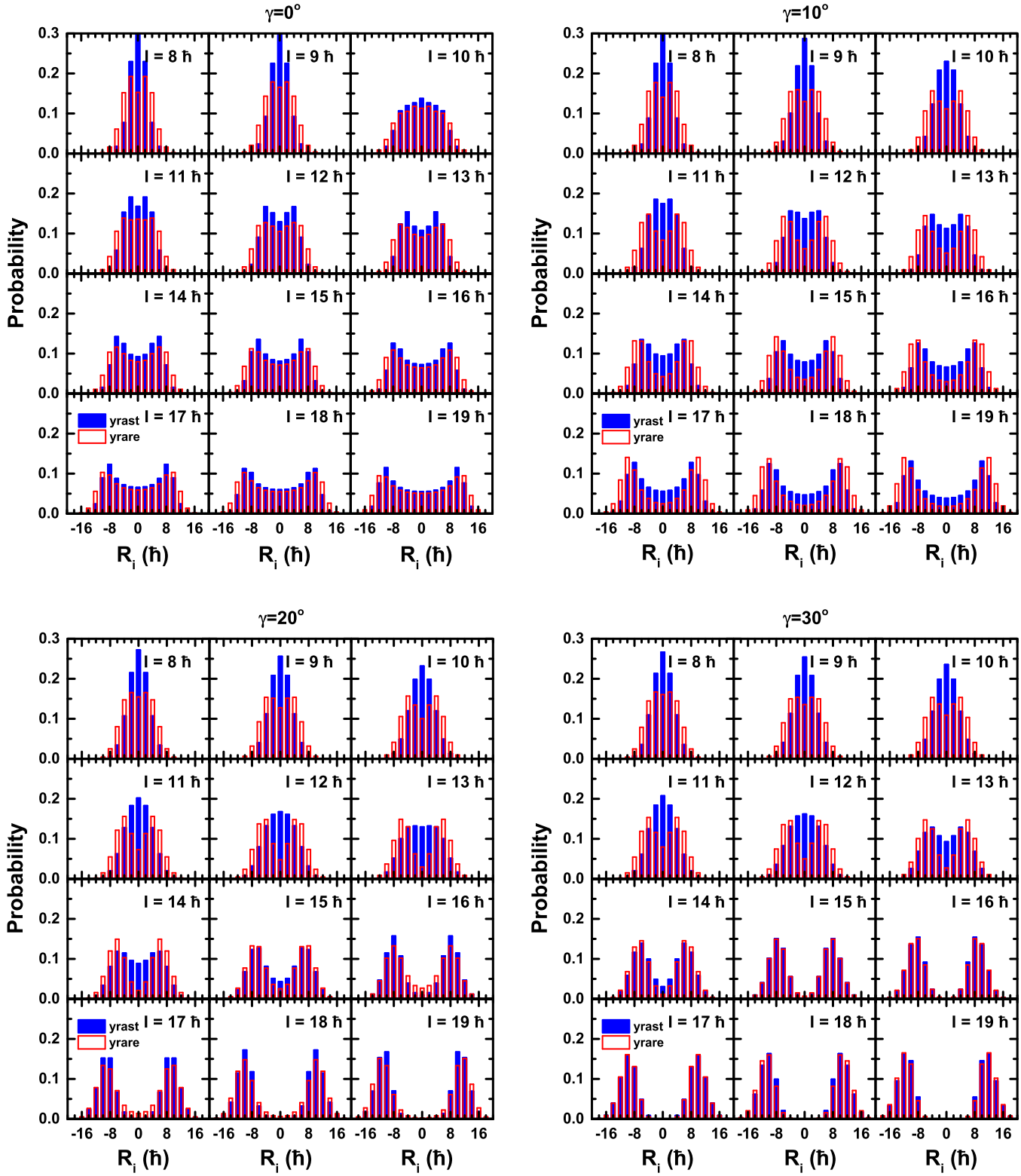

FIG. 6. Same as Fig. 4, but for the projection onto the i axis.

At $\gamma = 30^\circ$, the behavior of the P_{R_i} distribution is similar to that at $\gamma = 20^\circ$. It shows the picture of chiral vibration for $I \leqslant 12\hbar$ and chiral rotation for $I \geqslant 13\hbar$. In the spin region $15\hbar \leqslant I \leqslant 17\hbar$, one observes that the P_{R_i} distributions are indistinguishable. This provides the optimal situation for a chiral rotation.

V. SUMMARY

In this paper, we have investigated the behavior of the collective rotor in nuclear chiral motion (vibration or rotation) in the particle rotor model by transforming the rotational wave functions from the K representation to the R representation. After examining the energy spectra of the doublet bands as well as their energy differences as functions of the triaxial deformation parameter γ, the angular momentum components of the rotor, proton, neutron, and the total system have been studied in detail at $\gamma = 0^\circ$, 10°, 20°, and 30°. For this purpose, the probability distributions of the rotor angular momentum (R plots) and its projections onto the three principal axes (K_R plots) have been calculated and analyzed.

At $\gamma = 0^\circ$ and 10°, the behavior of the rotor in the yrast and yrare bands is different, and hence the angular momentum geometry does not support a chiral rotation. At $\gamma = 20^\circ$ and 30°, the evolution of the collective motion from chiral vibration at low spins to chiral rotation at high spins has been verified. In the spin region where chiral vibrations occur, the P_{R_i} distribution for the yrast band has only one peak at $R_i = 0\hbar$, while for the yrare band it has two peaks at nonzero R_i. In the spin region where chiral rotation occurs, the P_{R_i} distributions for the doublet bands are similar, having two peaks at nonzero R_i. Moreover, when the doublet bands become energetically degenerate, the behavior of the rotor is nearly the same.

To this end, one should note that the R and K_R plots presented in this work are not directly measurable quantities. Therefore, in the future we will use the R and K_R plots to calculate and examine the electromagnetic transition probabilities ($E2$ or $M1$) as fingerprints of chiral collective motions in triaxially deformed nuclei.

ACKNOWLEDGMENTS

Q.B.C. thanks E. Streck for help in setting up the numerical codes. Financial support for this work was provided by Deutsche Forschungsgemeinschaft (DFG) and National Natural Science Foundation of China (NSFC) through funds provided to the Sino-German CRC 110 "Symmetries and the Emergence of Structure in QCD" (DFG Grant No. TRR110 and NSFC Grant No. 11621131001), and the National Key R&D Program of China (Contracts No. 2018YFA0404400 and No. 2017YFE0116700). The work of U.-G.M. was also supported by the Chinese Academy of Sciences (CAS) through a President's International Fellowship Initiative (PIFI) (Grant No. 2018DM0034) and by the VolkswagenStiftung (DE) (Grant No. 93562).

[1] S. Frauendorf and J. Meng, Nucl. Phys. A **617**, 131 (1997).
[2] J. Meng and S. Q. Zhang, J. Phys. G: Nucl. Part. Phys. **37**, 064025 (2010).
[3] J. Meng, Q. B. Chen, and S. Q. Zhang, Int. J. Mod. Phys. E **23**, 1430016 (2014).
[4] R. A. Bark, E. O. Lieder, R. M. Lieder, E. A. Lawrie, J. J. Lawrie, S. P. Bvumbi, N. Y. Kheswa, S. S. Ntshangase, T. E. Madiba, P. L. Masiteng *et al.*, Int. J. Mod. Phys. E **23**, 1461001 (2014).
[5] J. Meng and P. W. Zhao, Phys. Scr. **91**, 053008 (2016).
[6] A. A. Raduta, Prog. Part. Nucl. Phys. **90**, 241 (2016).
[7] S. Frauendorf, Phys. Scr. **93**, 043003 (2018).
[8] B. W. Xiong and Y. Y. Wang, Atom. Data Nucl. Data Tables **125**, 193 (2019).
[9] J. Meng, J. Peng, S. Q. Zhang, and S.-G. Zhou, Phys. Rev. C **73**, 037303 (2006).
[10] A. D. Ayangeakaa, U. Garg, M. D. Anthony, S. Frauendorf, J. T. Matta, B. K. Nayak, D. Patel, Q. B. Chen, S. Q. Zhang, P. W. Zhao *et al.*, Phys. Rev. Lett. **110**, 172504 (2013).
[11] J. Peng, H. Sagawa, S. Q. Zhang, J. M. Yao, Y. Zhang, and J. Meng, Phys. Rev. C **77**, 024309 (2008).
[12] J. M. Yao, B. Qi, S. Q. Zhang, J. Peng, S. Y. Wang, and J. Meng, Phys. Rev. C **79**, 067302 (2009).
[13] J. Li, S. Q. Zhang, and J. Meng, Phys. Rev. C **83**, 037301 (2011).
[14] C. Droste, S. G. Rohozinski, K. Starosta, L. Prochniak, and E. Grodner, Eur. Phys. J. A **42**, 79 (2009).
[15] Q. B. Chen, J. M. Yao, S. Q. Zhang, and B. Qi, Phys. Rev. C **82**, 067302 (2010).
[16] I. Hamamoto, Phys. Rev. C **88**, 024327 (2013).
[17] D. Tonev, M. S. Yavahchova, N. Goutev, G. de Angelis, P. Petkov, R. K. Bhowmik, R. P. Singh, S. Muralithar, N. Madhavan, R. Kumar *et al.*, Phys. Rev. Lett. **112**, 052501 (2014).
[18] E. O. Lieder, R. M. Lieder, R. A. Bark, Q. B. Chen, S. Q. Zhang, J. Meng, E. A. Lawrie, J. J. Lawrie, S. P. Bvumbi, N. Y. Kheswa *et al.*, Phys. Rev. Lett. **112**, 202502 (2014).
[19] N. Rather, P. Datta, S. Chattopadhyay, S. Rajbanshi, A. Goswami, G. H. Bhat, J. A. Sheikh, S. Roy, R. Palit, S. Pal *et al.*, Phys. Rev. Lett. **112**, 202503 (2014).
[20] I. Kuti, Q. B. Chen, J. Timár, D. Sohler, S. Q. Zhang, Z. H. Zhang, P. W. Zhao, J. Meng, K. Starosta, T. Koike *et al.*, Phys. Rev. Lett. **113**, 032501 (2014).
[21] C. Liu, S. Y. Wang, R. A. Bark, S. Q. Zhang, J. Meng, B. Qi, P. Jones, S. M. Wyngaardt, J. Zhao, C. Xu *et al.*, Phys. Rev. Lett. **116**, 112501 (2016).
[22] H. Zhang and Q. B. Chen, Chin. Phys. C **40**, 024101 (2016).
[23] E. Grodner, J. Srebrny, C. Droste, L. Próchniak, S. G. Rohoziński, M. Kowalczyk, M. Ionescu-Bujor, C. A. Ur, K. Starosta, T. Ahn *et al.*, Phys. Rev. Lett. **120**, 022502 (2018).
[24] J. Li, Phys. Rev. C **97**, 034306 (2018).
[25] C. M. Petrache, B. F. Lv, A. Astier, E. Dupont, Y. K. Wang, S. Q. Zhang, P. W. Zhao, Z. X. Ren, J. Meng, P. T. Greenlees *et al.*, Phys. Rev. C **97**, 041304(R) (2018).
[26] Q. B. Chen, K. Starosta, and T. Koike, Phys. Rev. C **97**, 041303(R) (2018).
[27] B. Moon, C.-B. Moon, G. Dracoulis, R. Bark, A. Byrne, P. Davidson, G. Lane, T. Kibédi, A. Wilson, C. Yuan *et al.*, Phys. Lett. B **782**, 602 (2018).
[28] Q. B. Chen, B. F. Lv, C. M. Petrache, and J. Meng, Phys. Lett. B **782**, 744 (2018).
[29] T. Roy, G. Mukherjee, M. Asgar, S. Bhattacharyya, S. Bhattacharya, C. Bhattacharya, S. Bhattacharya, T. Ghosh, K. Banerjee, S. Kundu *et al.*, Phys. Lett. B **782**, 768 (2018).

[30] B. Qi, H. Jia, C. Liu, and S. Y. Wang, Phys. Rev. C **98**, 014305 (2018).
[31] J. Peng and Q. B. Chen, Phys. Rev. C **98**, 024320 (2018).
[32] Q. B. Chen and J. Meng, Phys. Rev. C **98**, 031303 (2018).
[33] M. Ionescu-Bujor, S. Aydin, N. Mărginean, C. Costache, D. Bucurescu, N. Florea, T. Glodariu, A. Ionescu, A. Iordăchescu, R. Mărginean *et al.*, Phys. Rev. C **98**, 054305 (2018).
[34] P. Olbratowski, J. Dobaczewski, J. Dudek, and W. Płóciennik, Phys. Rev. Lett. **93**, 052501 (2004).
[35] P. Olbratowski, J. Dobaczewski, and J. Dudek, Phys. Rev. C **73**, 054308 (2006).
[36] P. W. Zhao, Phys. Lett. B **773**, 1 (2017).
[37] R. Budaca, Phys. Rev. C **98**, 014303 (2018).
[38] S. Q. Zhang, B. Qi, S. Y. Wang, and J. Meng, Phys. Rev. C **75**, 044307 (2007).
[39] B. Qi, S. Q. Zhang, J. Meng, S. Y. Wang, and S. Frauendorf, Phys. Lett. B **675**, 175 (2009).
[40] B. Qi, S. Q. Zhang, S. Y. Wang, J. M. Yao, and J. Meng, Phys. Rev. C **79**, 041302(R) (2009).
[41] E. A. Lawrie and O. Shirinda, Phys. Lett. B **689**, 66 (2010).
[42] C. M. Petrache, Q. B. Chen, S. Guo, A. D. Ayangeakaa, U. Garg, J. T. Matta, B. K. Nayak, D. Patel, J. Meng, M. P. Carpenter *et al.*, Phys. Rev. C **94**, 064309 (2016).
[43] J. Peng, J. Meng, and S. Q. Zhang, Phys. Rev. C **68**, 044324 (2003).
[44] T. Koike, K. Starosta, and I. Hamamoto, Phys. Rev. Lett. **93**, 172502 (2004).
[45] T. Koike, K. Starosta, C. J. Chiara, D. B. Fossan, and D. R. LaFosse, Phys. Rev. C **67**, 044319 (2003).
[46] S. Y. Wang, S. Q. Zhang, B. Qi, and J. Meng, Phys. Rev. C **75**, 024309 (2007).
[47] S. Y. Wang, S. Q. Zhang, B. Qi, J. Peng, J. M. Yao, and J. Meng, Phys. Rev. C **77**, 034314 (2008).
[48] E. A. Lawrie, P. A. Vymers, J. J. Lawrie, C. Vieu, R. A. Bark, R. Lindsay, G. K. Mabala, S. M. Maliage, P. L. Masiteng, S. M. Mullins *et al.*, Phys. Rev. C **78**, 021305 (2008).
[49] O. Shirinda and E. A. Lawrie, Eur. Phys. J. A **48**, 118 (2012).
[50] B. Qi, S. Q. Zhang, S. Y. Wang, J. Meng, and T. Koike, Phys. Rev. C **83**, 034303 (2011).
[51] B. Qi, H. Jia, N. B. Zhang, C. Liu, and S. Y. Wang, Phys. Rev. C **88**, 027302 (2013).
[52] A. Bohr and B. R. Mottelson, *Nuclear Structure*, Vol. II (Benjamin, New York, 1975).
[53] P. Ring and P. Schuck, *The Nuclear Many Body Problem* (Springer Verlag, Berlin, 1980).
[54] E. Streck, Q. B. Chen, N. Kaiser, and Ulf-G. Meißner, Phys. Rev. C **98**, 044314 (2018).
[55] C. N. Davids and H. Esbensen, Phys. Rev. C **69**, 034314 (2004).
[56] S. Modi, M. Patial, P. Arumugam, E. Maglione, and L. S. Ferreira, Phys. Rev. C **95**, 024326 (2017).
[57] A. S. Davydov and G. F. Filippov, Nucl. Phys. **8**, 237 (1958).